

High-sensitivity diamond magnetometer with nanoscale resolution

J. M. TAYLOR^{1*}, P. CAPPELLARO^{2,3*}, L. CHILDRESS^{2,4}, L. JIANG², D. BUDKER⁵, P. R. HEMMER⁶,
A. YACOBY², R. WALSWORTH^{2,3} AND M. D. LUKIN^{2,3†}

¹Department of Physics, Massachusetts Institute of Technology, Cambridge, Massachusetts 02139, USA

²Department of Physics, Harvard University, Cambridge, Massachusetts 02138, USA

³Harvard-Smithsonian Center for Astrophysics, Cambridge, Massachusetts 02138, USA

⁴Department of Physics, Bates College, Lewiston, Maine 04240, USA

⁵Department of Physics, University of California, Berkeley, California 94720, USA

⁶Department of Electrical and Computer Engineering, Texas A&M University, College Station, Texas 77843, USA

*These authors contributed equally to this work

†e-mail: lukin@physics.harvard.edu

Published online: 14 September 2008; doi:10.1038/nphys1075

The detection of weak magnetic fields with high spatial resolution is an important problem in diverse areas ranging from fundamental physics and material science to data storage and biomedical science. Here, we explore a novel approach to the detection of weak magnetic fields that takes advantage of recently developed techniques for the coherent control of solid-state electron spin quantum bits. Specifically, we investigate a magnetic sensor based on nitrogen-vacancy centres in room-temperature diamond. We discuss two important applications of this technique: a nanoscale magnetometer that could potentially detect precession of single nuclear spins and an optical magnetic-field imager combining spatial resolution ranging from micrometres to millimetres with a sensitivity approaching a few fT Hz^{-1/2}.

Over the past few decades, a wide variety of magnetic sensors have been developed using approaches including superconducting quantum interference devices¹ (SQUIDs), the Hall effect in semiconductors², atomic vapour and Bose–Einstein condensate based magnetometry^{3–8} and magnetic resonance force microscopy^{9–11}. Here, we present a novel approach to high-spatial-resolution magnetic-field detection, using systems currently explored as quantum bits: isolated electronic spins in a solid. We focus on spins associated with nitrogen-vacancy colour centres in diamond¹² (Fig. 1a,b), because they can be individually addressed, optically polarized and detected, and exhibit excellent coherence properties even at room temperature^{13–15}. Recently, coherent control of nitrogen-vacancy electronic spin qubits has been used to sense and manipulate nearby individual electronic^{16,17} and nuclear spins¹⁸ in a diamond lattice. In what follows, we describe how such a system can also be used for the precision sensing and imaging of external magnetic fields.

We discuss two types of potential implementation of such sensors. First, a single sensing spin confined in a nanoscale region can be brought in direct proximity to a magnetic-field source, such as an electron or nuclear spin. For example, a diamond nanocrystal (10–20 nm in size) containing a single nitrogen-vacancy centre can be attached to a tip of a scanning probe¹⁹ (Fig. 1c) such as that of an atomic force microscope. Second, a bulk diamond sample with a high density of nitrogen-vacancy centres can be used to sense fields created by remote objects with ultrahigh sensitivity and submicrometre spatial resolution (Fig. 1d).

MAGNETOMETRY WITH SINGLE ELECTRONIC SPIN QUBITS

The operating principles of our approach are closely related to those of magnetometers based on spin precession in atomic vapours. In particular, detecting the relative energy shift induced by a magnetic field b between two Zeeman sublevels enables precise determination of an applied d.c. or a.c. magnetic field. Ultimately, sensitivity is determined by the spin coherence time and by the spin projection noise. Although solid-state electronic spins have shorter coherence times than gaseous atoms, quantum control techniques can decouple them from the local environment and from each other, as we show below, leading to a substantial improvement in their sensitivity to external, time-varying magnetic fields, while retaining the desirable features of a robust solid sensor.

The canonical approach to detecting a Zeeman shift uses a Ramsey-type sequence as shown in Fig. 2a. A $\pi/2$ -pulse creates a superposition of two Zeeman levels, which acquire a relative phase $\phi \propto (g\mu_B/\hbar)b\tau$ from the external field b during the free evolution interval τ (here μ_B is the Bohr magneton and $g \approx 2$ for nitrogen-vacancy centres). Another $\pi/2$ -pulse transforms the relative phase into a population difference, which is measured optically and from which the Zeeman shift is inferred. For small ϕ , the magnetometer signal \mathcal{S} (proportional to the induced population difference) depends linearly on the magnetic field: $\mathcal{S} \approx (g\mu_B/\hbar)b\tau$. During the total averaging interval T , T/τ measurements can be made, yielding a shot-noise-limited sensitivity η given by the minimum detectable field, $b_{\min} \equiv \eta/\sqrt{T} \approx (\hbar/g\mu_B)(1/\sqrt{\tau T})$.

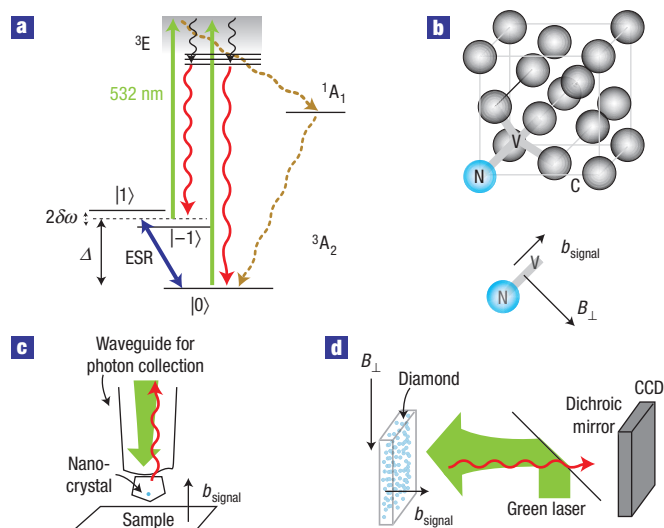


Figure 1 Overview of a diamond-based magnetometer. **a**, Level structure of a single nitrogen-vacancy centre. The nitrogen-vacancy centre's ground state is a spin triplet with a $\Delta = 2.87$ GHz crystal field splitting and a Zeeman shift $\delta\omega$. Under the application of green light (~ 532 nm), the nitrogen-vacancy centre initially exhibits spin-dependent photoluminescence, even at room temperature, enabling optical detection of electronic spin resonance. After continued illumination, the nitrogen-vacancy spin is pumped into the ground state $m_s = 0$. **b**, Crystal structure of diamond with a (111) nitrogen-vacancy centre. A static bias field B_\perp is applied perpendicular to the 111 axis, and small magnetic fields aligned with the 111 axis are detected as the signal. **c**, A nanocrystal of diamond at the end of a waveguide for photon collection, with resolution limited by the size of the crystal. **d**, A macroscopic sample of diamond, with resolution limited by optics, enables high spatial resolution and signal-to-noise. A green laser produces spin-dependent photoluminescence, detected by measuring red light imaged onto a CCD.

Increasing the interrogation time τ improves the sensitivity until random (environmental) perturbations lead to decay of the free-precession signal. In the case of solid-state spin systems, the coherence is limited by interactions with nearby lattice nuclei and paramagnetic impurities, resulting in an ensemble dephasing time T_2^* . Furthermore, there will be a finite number of fluorescence photons collected and detected, leading to extra photon shot noise, and a finite contrast to the Ramsey fringes. We describe these effects by a single parameter $C \leq 1$, which approaches unity for ideal, single-shot readout (see Methods section). The optimum sensitivity of a magnetometer based on a single electronic spin, achieved for $\tau \sim T_2^*$, is given by

$$\eta_{\text{d.c.}} \approx \frac{\hbar}{g\mu_B C \sqrt{T_2^*}}.$$

For current experiments¹⁵, with detection efficiency $\sim 10^{-3}$, $C \approx 0.05$ and $T_2^* \sim 1 \mu\text{s}$. This yields an optimal sensitivity $\sim 1 \mu\text{T Hz}^{-1/2}$. Improving the collection efficiency by using a tapered fibre or a plasmonic waveguide²⁰ to $\eta \sim 5\%$ yields $C \approx 0.3$ and leads to a sensitivity $\sim 120 \text{ nT Hz}^{-1/2}$.

Coherent control techniques can improve the sensitivity for a.c. fields. Owing to the long correlation times characteristic of dipolar interactions between spins in systems such as diamond—the principal source of dephasing—spin echo techniques can markedly extend the coherence time. Specifically, by adding an extra microwave π pulse to the Ramsey sequence at time $\tau/2$, the Hahn echo sequence (Fig. 2a) removes the effect of environmental

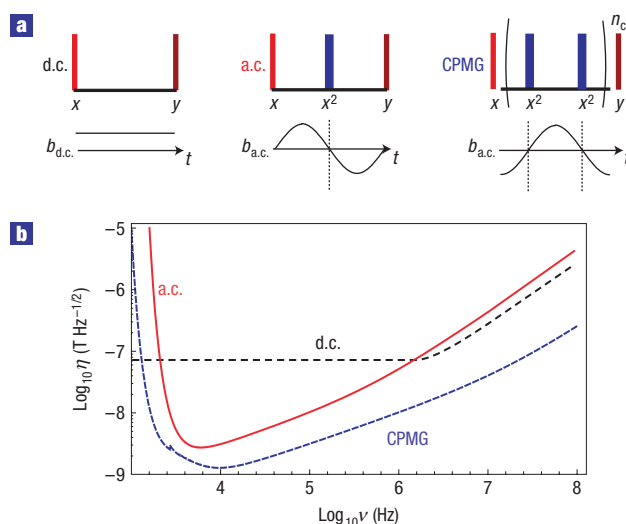


Figure 2 Control sequences for various operation modes of the magnetometer and corresponding sensitivities to magnetic fields. **a**, ESR pulse sequences for magnetometry, where x and y indicate the linear polarization of the ESR pulse in the laboratory frame. Left: Ramsey pulse sequence for d.c.-field measurement. Middle: Echo-based pulse sequence for a.c. magnetometry $\pi/2|_x - \pi|_x - \pi/2|_y$. Right: CPMG-based pulse sequence for improved a.c. magnetometry $\pi/2|_x(-\pi|_x - \pi|_x - \pi/2|_y)$, where n_c is the number of repetitions of the paired π pulses. For small accumulated phases, a signal linear in the field can also be obtained with all pulses along the x direction if a reference field $B_{\text{ref}} \sin(2\pi t/\tau)$ is added. **b**, d.c. and a.c. sensitivity to magnetic fields for a single nitrogen-vacancy centre as a function of signal frequency, ν . Also shown is the expected performance of CPMG composite pulse sequences, with the optimum n_c as described in Methods section. Parameters used assume carbon-13-limited coherence with $T_2^* = 1 \mu\text{s}$ (ref. 13), $T_2 = 300 \mu\text{s}$ (ref. 15), $t_m = 1 \mu\text{s}$, $C = 0.3$, $T_1 = 20 \text{ ms}$ (ref. 18) and an error per pulse of 1%.

perturbations with a correlation time that is long compared with τ . Thus, a signal field $b(t)$ oscillating in-phase with the pulse sequence produces an overall additive phase shift, leading to a total phase accumulation, $\delta\phi = (g\mu_B/\hbar)[\int_0^{\tau/2} b(t) dt - \int_{\tau/2}^{\tau} b(t) dt]$. For a signal field of frequency ν and initial phase ϕ_0 , $b(t) = b \sin(\nu t + \phi_0)$, this yields $\delta\phi = (g\mu_B/\hbar) b \tau f(\nu\tau, \phi_0)$, with $f(x, \phi_0) = (\sin^2(x/4) \cos(x/2 + \phi_0)/x/4)$. In essence, the spin echo enables us to extend the interrogation time τ from the limit set by T_2^* up to a value T_2 that is close to the intrinsic spin coherence time, at the cost of a reduced bandwidth and insensitivity to frequencies $\lesssim 1/T_2$. For maximal response to continuous-wave signals with known frequency and phase (assuming small b), we find $\tau = 2\pi/\nu$ and $\phi_0 = 0$ to be optimal. For signals with a time dependence that is *a priori* unknown, it is useful to measure the signal variance, which provides equivalent performance (see Methods section). In either case, the sensitivity is improved by $\approx \sqrt{T_2^*/T_2}$:

$$\eta_{\text{a.c.}} \approx \frac{\pi\hbar}{2g\mu_B C \sqrt{T_2^*}}.$$

The optimum sensitivity is achieved only for fields oscillating near $\nu \sim 1/T_2$. However, these results can be easily extended to higher frequency signals. In particular, for signal field oscillation periods shorter than the dephasing time, the interrogation time need not be restricted to the duration of one period, but can be multiples of it. Then, composite pulse sequences such as the Carr–Purcell–Meiboom–Gill²¹ (CPMG) sequence may perform

better at the expense of a reduced bandwidth. Furthermore, in ultrapure samples where nuclear spins' evolution leads to decay of the echo signal, the long correlation time of the nuclei leads to non-exponential decay of the echo signal^{22,23}. In this case, the CPMG sequence can increase the interrogation time, further reducing the minimum detectable field (see Fig. 2 and Methods section). Finally, another way to improve the magnetometer sensitivity is to use many sensing spins, where we can take advantage of the relatively high achievable density of spins in the solid-state ($\sim 10^{17} \text{ cm}^{-3}$) compared with atomic magnetometers ($\sim 10^{13} \text{ cm}^{-3}$) (ref. 24).

IMPLEMENTATION WITH NITROGEN-VACANCY CENTRES

We now discuss specific details of magnetometry using nitrogen-vacancy centres in diamond, developing an appropriate operating regime and determining the optimal sensitivities possible for current experimental technology. The fine structure of the electronic ground state of a nitrogen-vacancy centre, shown in Fig. 1a, is a spin triplet. The crystal field splits the $m_s = \pm 1$ Zeeman sublevels from the $m_s = 0$ sublevel by $\Delta = 2\pi \times 2.87 \text{ GHz}$, enabling the use of electron-spin resonance (ESR) techniques even at vanishing external magnetic field. Furthermore, under application of green light, nitrogen-vacancy centres exhibit a transient, spin-dependent fluorescence, which enables optical detection of the spin. After the transient signal decays, the system optically pumps into the $m_s = 0$ state, which prepares the system for the next measurement (see Methods section).

As a specific example, we focus on magnetometry in low external static magnetic fields ($\leq 10 \text{ mT}$). In this case, Δ is the largest energy scale and sets the spin quantization axis parallel to the nitrogen-to-vacancy direction. The secular Hamiltonian, including a small external field $\mathbf{B}(t) = (B_x, B_y, B_z)$, is

$$\mathcal{H} = \hbar \Delta S_z^2 + g\mu_B B_z S_z,$$

where B_z is the component of the magnetic field along the nitrogen-vacancy-centre's axis and S_z takes the values $m_s = 0, \pm 1$. Terms proportional to the perpendicular field are suppressed to order $\sim B_{x,y}^2/\Delta$ and do not depend on the field B_z being measured, and therefore may be neglected.

At low magnetic fields, the $m_s = \pm 1$ manifold can be used to implement a vector magnetometer, sensitive only to components of the magnetic field along the centre's axis. We focus on the $m_s = \pm 1$ manifold as it has twice the energy splitting of the 0–1 manifold and is less affected by nuclear spin-induced decoherence at low fields, because internuclear interactions are suppressed by the large hyperfine field²⁵.

Coherent control of the nitrogen-vacancy-centre's spin states is obtained using an ESR magnetic field oscillating at angular frequency Δ . ESR pulses linearly polarized along the x axis rotate the nitrogen-vacancy spin between the two-dimensional subspace of $|0\rangle$ and $|+\rangle = (|1\rangle + |-1\rangle)/\sqrt{2}$. To manipulate $|\pm 1\rangle$ superpositions, extra control can be provided by a background oscillating reference field $[B_{\text{ref}} \sin(2\pi t/\tau)]$ along the z axis. Specifically, $B_{\text{ref}} = (\hbar/g\mu_B)\pi^2/8\tau$ yields an optimal phase offset to achieve a magnetometer signal linear in the field strength (Fig. 2).

The sensitivity as a function of the signal frequency for both a.c. and d.c. detection is plotted in Fig. 2. For diamonds where natural abundance (1.1%) carbon-13 nuclei are the principal cause of dephasing, $T_2^* \sim 1 \mu\text{s}$ and $T_2 \sim 300 \mu\text{s}$ (ref. 18). Again using current experimental parameters, with $C \approx 0.05$, and measurement and preparation time $t_m \leq 2 \mu\text{s}$, we can optimize the sensitivity as a function of τ . Including corrections from decoherence with expected signal decay (see Methods section) $\propto \exp[-(\tau/T_2)^3]$,

we find: $\eta_{\text{a.c.}} = (\pi\hbar/2g\mu_B)e^{(\tau/T_2)^3}\sqrt{\tau+t_m}/C\tau$. We obtain optimal sensitivity of $\eta_{\text{a.c.}} \approx 18 \text{ nT Hz}^{-1/2}$ for a single nitrogen-vacancy centre using current experimental collection efficiencies. Improved collection efficiencies ($C = 0.3$) would yield $\eta_{\text{a.c.}} = 3 \text{ nT Hz}^{-1/2}$. Note that spin T_1 relaxation occurs on timescales much longer than milliseconds and may be safely neglected¹⁸. Finally, the observed dephasing times are independent of temperature from 4 to 300 K, owing in part to the vanishing polarization of the nuclear bath at small magnetic fields.

When more than one nitrogen vacancy centre exists in the sample, they can belong to four different crystallographic classes, each corresponding to the centres' alignments along different (111) axes. To operate as a vector magnetometer along a controlled direction, a transverse (d.c.) magnetic field $B_{\perp} \geq 0.3 \text{ mT}$ (see Methods section) detunes the other three classes' levels such that the ESR field used for quantum control excites only spins with the desired crystallographic orientation, perpendicular to the external field. Thus, one in four spins contributes to the magnetometer signal.

MAGNETOMETRY IN THE HIGH-DENSITY LIMIT

A principle advantage of our approach over other spin precession magnetometers is the high achievable density n of sensing spins. This improves the sensitivity to fields that are homogeneous over the magnetometer volume, because the projection noise per unit volume decreases as $1/\sqrt{n}$. Nitrogen-vacancy centres can be created in controlled densities by implanting high-purity diamond with nitrogen ions and subsequently annealing the sample to recombine the nitrogen with vacancies²⁶. Assuming an initial nitrogen concentration $\sim 10^{18} \text{ cm}^{-3}$ with a conversion $f \sim 0.1$ to nitrogen-vacancy centres^{17,26,27}, we expect it will be feasible to create diamond crystals with a nitrogen-vacancy-centre density exceeding $\sim 10^{17} \text{ cm}^{-3}$, with an average distance between centres of less than 10 nm. Even at these densities, effects such as superradiance do not have a role owing to the large spectral width of the nitrogen-vacancy fluorescence.

At high spin densities, nitrogen-vacancy paramagnetic impurities and nitrogen-vacancy/nitrogen-vacancy interactions may limit the sensitivity of the magnetometer. In particular, substitutional nitrogen impurities with one bound electron (P1 centres) become a sizable source of dephasing in high-density samples^{28,29}. The dipole–dipole interaction between these centres has a characteristic timescale $T_c \equiv (1/\alpha n_{\text{epi}})$, where α is of the order of the dipole coupling between electron spins, $(\mu_0/4\pi)(g\mu_B)^2/\hbar \approx 3.3 \times 10^{-13} \text{ s}^{-1} \text{ cm}^3$ and n_{epi} is the density of paramagnetic impurities. Qualitatively, this timescale corresponds to the rotation time of a single paramagnetic spin in the presence of the random field from the other paramagnetic centres. The timescale for interaction between this impurity bath and a given nitrogen-vacancy centre will be of the same order of magnitude. This suggests an exponential decay of spin echo coherence on a timescale T_c (see Methods section), in contrast to single nitrogen-vacancy-centre-based sensing, where nearby nuclear spins limit the coherence time.

To evaluate the effects of paramagnetic impurities, we assume a density n of nitrogen-vacancy centres and $n_{\text{epi}} = n(1-f)/f$ of paramagnetic impurities, where f is the conversion factor described above. The relevant figure of merit is the sensitivity per root volume $\eta_{\text{a.c.}}^V = \eta_{\text{a.c.}}\sqrt{V}$. We find

$$\eta_{\text{a.c.}}^V = \frac{\hbar}{g\mu_B} \frac{\pi e^{(\tau/T_{2,\text{Carbon}})^3}}{C\sqrt{n}\tau} \times e^{\tau/T_c},$$

where we have taken into account that the sensing centres account for only one fourth of the nitrogen-vacancy centres

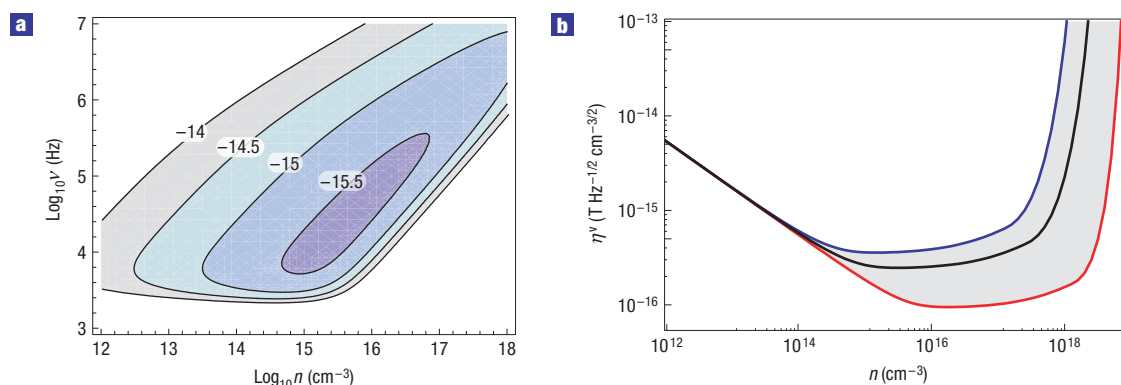


Figure 3 Sensitivity per root volume ($\eta^V_{\text{a.c.}}$) at high nitrogen-vacancy-centre density, for the a.c.-field echo measurement scheme. **a**, Contour plot of $\log_{10} \eta^V$ in $\text{T Hz}^{-1/2} \text{cm}^{3/2}$ as a function of nitrogen-vacancy-centre density and signal field frequency. **b**, Sensitivity at the optimal field frequency, as a function of nitrogen-vacancy-centre density; the black curve is the sensitivity for $f = 0.1$, whereas the blue and red curves are for $f = 0.05$ (higher paramagnetic impurity density) and 0.5 (lower paramagnetic impurity density), respectively. Parameters used correspond to $T_{2,\text{carbon}} = 300 \mu\text{s}$ (ref. 15), $t_m = 1 \mu\text{s}$, $C = 0.3$ and $\alpha = 3.3 \times 10^{-13} \text{s}^{-1} \text{cm}^3$.

in the sample. Here, we include both dephasing due to a bath of dipolar-coupled nuclear spins and the paramagnetic spin bath just discussed. In the high nitrogen-vacancy density and low- f regime, $T_{2,\text{Carbon}} > T_c > T_2^*$, that is, carbon-13 is no longer the limit to echo lifetimes, but still limits inhomogeneous broadening. Then the optimum magnetometer sensitivity becomes: $\tilde{\eta}^V_{\text{a.c.}} = (\hbar\pi/g\mu_B C)\sqrt{2\alpha e(1-f)/f}$. For $f = 0.1$ and $T_{2,\text{Carbon}} = 300 \mu\text{s}$, the optimum sensitivity is independent of the nitrogen-vacancy density over the range $n \simeq 10^{15} - 10^{17} \text{cm}^{-3}$, as is seen in Fig. 3a, and reaches a maximum sensitivity value $\tilde{\eta}^V_{\text{a.c.}} \sim 250 \text{aT Hz}^{-1/2} \text{cm}^{-3/2}$ for $C = 0.3$. However, the optimum echo time depends on the nitrogen-vacancy density, $\tau = f/[(1-f)2n\alpha]$, with higher density samples requiring higher detection frequencies. Finally, for $n \gg 10^{17} \text{cm}^{-3}$, corrections due to finite preparation, control and measurement times can become important, and lead to the limitations in sensitivity at high nitrogen-vacancy density seen in Fig. 3a.

To push the sensitivity limits beyond the cutoff imposed by paramagnetic impurities, we can exploit more advanced forms of dynamical decoupling³⁰ than spin echo. With appropriate external time-dependent controls, the system can be made to evolve under an effective, time-averaged Hamiltonian that is a suitable symmetrization of the undesired interactions. For example, driving the P1 centres through spin resonance at a rate much faster than the intrinsic decorrelation time, T_c , acts as a rapid spin echo for the nitrogen-vacancy centres without affecting the nitrogen-vacancy-centre's magnetic-field-sensing capabilities. Furthermore, improving implantation and conversion techniques (by optimizing implant energies²⁷ or by using cold implantation³¹) could increase the ratio of nitrogen-vacancy centres to paramagnetic impurities. When the conversion efficiency exceeds 50%, interactions between nitrogen-vacancy centres become the primary source of noise, with a dephasing³² $\propto (\alpha n \tau)^2$. The coupling between the sensing nitrogen-vacancy centres is a $S_{j,z}S_{k,z}$ interaction that is not removed with spin echo. However, by using collective rotations driven by appropriate ESR pulses, the interaction can be successively rotated through the x , y and z axes for an equal time duration³³; so that on average the spins will experience an isotropic Hamiltonian, which commutes with the signal perturbation and thus allows the spin evolution necessary for magnetometry³⁴. Pulse sequences such as MREV^{35,36} (an eight-pulse refocusing sequence introduced by Mansfield, Rhim, Ellis and

Vaughan) can induce the desired evolution, and will be necessary in the high nitrogen-vacancy-centre density limit.

SINGLE-SPIN DETECTION WITH A NANO-MAGNETOMETER

Nitrogen-vacancy magnetometers can be applied to an outstanding challenge in magnetic sensing: the detection and real-space imaging of small ensembles of electronic and nuclear spins, with the long-term goal of resolving individual nuclear spins in a molecule. As the magnetic field from a single dipole decreases with distance as $\sim 1/r^3$, a magnetometer that can be brought into close proximity of the field source offers a clear advantage. A diamond nanocrystal or a single nitrogen-vacancy centre near the surface of a bulk crystal within a scanning set-up^{37–39} would enable a spatial resolution limited only by the distance between the nitrogen-vacancy centre and the object of study, not by the wavelength of the fluorescence signal. For example, consider a prototype system consisting of a crystal with a single nitrogen-vacancy centre at a distance $r_0 \sim 10 \text{nm}$ from the surface of the crystal. At this distance, the dipolar field from a single proton is $B_H \simeq 3 \text{nT}$, which is well within the projected limits for a single nitrogen-vacancy centre.

To examine a practical method to measure the magnetic field from a single spin, we consider a material with a varying nuclear spin density n_s that is brought in close proximity (a distance $\sim r_0$) to the nitrogen-vacancy centre. At realistic temperatures, the thermal nuclear spin polarization of the material will be small. However, because only a few spins are involved, the distribution of spin configurations leads a large variance in the spin polarization⁴⁰, providing a substantial, albeit randomly oriented, magnetic field to be detected by the nitrogen-vacancy magnetometer. We find (see Methods section) that the field magnitude measured by our sensor will be characterized by a variance $B_{\text{r.m.s.}} \sim B_H \sqrt{N}$, where $N \sim 8\pi n_s r_0^3$ is the effective number of spins contributing to the signal. This indicates that our prototype system has an effective spatial resolution determined only by the distance of the nitrogen-vacancy centre from the surface of the sample material, assuming we can position the sensor relative to the sample with stability much better than r_0 .

At nuclear spin densities $\lesssim 10^{18} \text{cm}^{-3}$, there is on average one or fewer nuclear spins in an effective sensing volume with $r_0 \sim 10 \text{nm}$. Hence, in this case, single spins could be measured. However, most organic molecules have substantially higher proton densities

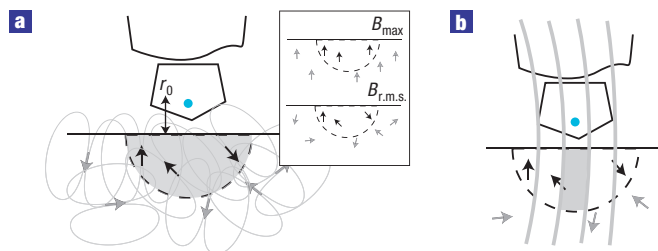


Figure 4 Illustration of high-spatial-resolution magnetometry with a diamond nanocrystal. **a**, The dipolar fields from spins in the sample decay rapidly with distance; only those within a distance $\sim r_0$ contribute to the observable signal for a point-like detector (such as a single nitrogen-vacancy centre in a nanocrystal, shown by the blue dot). The inset shows how B_{\max} and $B_{r.m.s.}$ are related; when few spins are involved, the statistical fluctuations become large. **b**, In the presence of a magnetic-field gradient (field lines in grey), only a small region of the detection volume is precessing at the frequency band centre of the detector, enabling even higher spatial resolution.

($\sim 10^{22}$ – 10^{23} cm $^{-3}$). To measure only one proton at a time would require a further improvement in spatial resolution. In this case, a magnetic-field gradient can be used, which enables conversion of high spectral resolution to high spatial resolution. Using similar techniques to those used in magnetic force resonance microscopy⁹, a magnet near the surface of a substrate can produce gradient fields of $\geq 10^6$ T m $^{-1}$ (Fig. 4b). The narrow bandwidth of our detector, ~ 4 kHz ($\sim 1/T_2$), enables it to spectrally distinguish two protons separated by a magnetic-field difference of 0.1 mT, corresponding to physical separation of 0.1 nm. This implies that individual proton detection may be possible even in organic and biological molecules. The narrow bandwidth associated in particular with the CPMG approach (see Methods section) enables different isotopes to be distinguished, owing to their unique gyromagnetic ratios. More generally, our approach enables the detection of nanoscale variations in the chemical and physical environment.

We note that the present approach can surpass the sensitivity of SQUID¹, Hall-bar² and recently proposed optically-pumped semiconductor-based⁴¹ nano-magnetometers by more than an order of magnitude, with 10–2,000 times better spatial resolution. The ultimate limits to miniaturization of nitrogen-vacancy-centre nano-magnetometers, which are probably due to surface effects, are not yet well understood.

IMAGING OF MACROSCOPIC MAGNETIC FIELDS

In contrast to the nano-magnetometer approach outlined above, a macroscopic crystal of diamond containing many nitrogen-vacancy centres may be used as a high-sensitivity imaging magnetometer with large field-of-view and optical wavelength-limited spatial resolution. As an example system, we consider a crystal of diamond with a high density of nitrogen-vacancy centres. The signal from nitrogen-vacancy centres in a diffraction-limited setting, where a CCD (charge-coupled device) might be used to image the crystal, is divided into separate ‘pixels’, with each pixel corresponding to a $\sim (1 \mu\text{m})^3$ volume element of the crystal. For nitrogen-vacancy-centre densities of $\sim 10^{15}$ – 10^{17} cm $^{-3}$ and $C = 0.3$, each pixel would have ~ 100 pT Hz $^{-1/2}$ a.c. sensitivity. This spatial resolution is comparable to micro-SQUID magnetometers but with four orders of magnitude higher magnetic-field sensitivity⁴². In such a scenario, diamond crystals could range from tens of micrometres to millimetres in size, and be physically

integrated with fibre-based optics for a robust and practical magnetic-field imager.

Larger detector volumes further improve the sensitivity for whole-sample measurements. For example, a $(3 \text{ mm})^2 \times 1 \text{ mm}$ thick crystal can achieve an overall sensitivity of 3 fT Hz $^{-1/2}$ with millimetre resolution. Reducing the ratio of paramagnetic impurities to nitrogen-vacancy centres could potentially lead to the detection of attotesla fields, opening the prospect of improved tests of fundamental symmetries and physical laws.

The high magnetic-field sensitivity in a small volume offered by solid-state spin qubits such as nitrogen-vacancy centres in diamond can find a wide range of applications, from fundamental physics tests or quantum computing applications to detection of NMR signals, surface physics and material science, and medical imaging and biomagnetism. Recently, proof-of-principle experimental demonstrations of such a sensor have been carried out by members of our collaboration⁴³ and other groups⁴⁴. Further extensions could include the use of non-classical spin states, such as squeezed states induced by the spin–spin coupling. The sensitivity could also be improved by using synthesized, isotopically purified diamond containing a lower fraction of carbon-13, the main cause of dephasing at moderate nitrogen-vacancy densities, and by developing more efficient nitrogen-vacancy-centre creation techniques that do not result in high densities of paramagnetic impurities. On a more general level, these ideas could apply to a variety of paramagnetic systems or other types of solid-state qubit that are sensitive to different perturbations.

METHODS

ESR CONTROL TECHNIQUES

The spin triplet of the nitrogen-vacancy centre has a V-type level configuration. An external microwave field tuned to the $\Delta = 2.87$ GHz resonance with its magnetic field linearly polarized along the x axis drives transitions between $|0\rangle$ and the superposition $|+\rangle = (|1\rangle + |-1\rangle)/\sqrt{2}$, whereas the state $|-\rangle = (|1\rangle - |-1\rangle)/\sqrt{2}$ is dark—it is decoupled from the field owing to destructive quantum interference. Application of a magnetic field aligned with the nitrogen-vacancy-centre z -axis perturbs the interference, and enables complete quantum control of the spin triplet. In an echo sequence appropriate for magnetometry using the $|+\rangle$ and $|-\rangle$ states, the traditional $\pi/2 - \pi - \pi/2$ structure is replaced by $\pi - 2\pi - \pi$: the first pulse creates $|+\rangle$, the second induces a relative π -phase shift between $|+\rangle$ and $|-\rangle$ and the third converts $|+\rangle$ to $|0\rangle$ while leaving $|-\rangle$ population trapped in the $m_s = \pm 1$ manifold. We remark that for external fields in excess of a few milliteslas it may be more convenient to use the 0–1 manifold, as two different resonance frequencies would be necessary for using the ± 1 manifold in this regime.

A.C.-FIELD MEASUREMENT SCHEME AND BANDWIDTH

a.c.-field detection requires synchronization of the pulse sequence with the external magnetic-field oscillations. When this is not practical or if the field phase φ_0 varies randomly in time, successive measurements will give random readings distributed over the range of the function $f(v\tau, \varphi_0)$ (given in the main text) resulting in a zero average signal. In this situation, information about the field intensity is contained in the measured signal variance, provided the random phase correlation time τ_φ satisfies: $\tau \ll \tau_\varphi < T$. (If $\tau_\varphi > T$, the total averaging time, the scheme presented in the main text could be used.) For $\tau = 2\pi/\nu$ and a uniformly distributed φ_0 , $\langle f(2\pi, \varphi_0)^2 \rangle = 2/\pi^2$ and the standard deviation of the measured signal is: $(g\mu_B\sqrt{2}/\hbar\pi)b\tau$, whereas the noise has a contribution from the uncertainty in the variance equal to $2^{1/4}/\pi$. The sensitivity is thus worsened only by a factor $\sqrt{2(1 + \sqrt{2}/\pi^2)} \approx 1.5$ compared with detection of a signal with a known phase.

To increase the sensitivity at higher frequencies, it is possible to increase the interrogation time (see the main text) by using a series of 2π -pulse cycles (CPMG pulse sequence). A single cycle corresponds to the pulse sequence $\tau/4 - \pi - \tau/2 - \pi - \tau/4$. Although this method increases the sensitivity, the measurement bandwidth decreases with increasing cycle number n_c . The a.c. magnetometer response to a general signal $b(t)$ can be calculated from a frequency space analysis: $(1/2\pi)\int_{-\infty}^{\infty} \tilde{b}(\omega)(\int_0^{\tau/2} e^{i\omega t} dt - \int_{\tau/2}^{\tau} e^{i\omega t} dt) d\omega = (\tau/2\pi)\int_{-\infty}^{\infty} \tilde{b}(\omega)W_0(\omega,\tau)e^{i\omega\tau/2} d\omega$, where $\tilde{b}(\omega)$ is the Fourier transform

of the signal field and W_0 a windowing function. With a similar calculation, we obtain the windowing function for an n_c -cycle pulse sequence:

$$W_{n_c}(\omega, \tau) = \frac{1 - \sec(\tau\omega/4)}{\tau\omega/2} \sin(n_c\tau\omega/2).$$

This function has a band centre $\approx 2\pi/\tau$ and bandwidth (half-width at half-maximum) $\sim 4/(n_c\tau)$.

We can evaluate the improvement in coherence times for the CPMG sequence in cases where a detailed understanding of the main source of decoherence is available. For the single-spin magnetometer, we can approximate the nuclear spin environment by separating contributions from distant nuclear spins, undergoing dipolar spin diffusion, and nearby nuclear spins, the evolution of which is frozen by the electron spin's dipolar field^{22,23}. We can model the distant nuclear spins as an exponentially correlated Gaussian fluctuating field \tilde{B} with a correlation function $\langle \tilde{B}(t)\tilde{B}(t') \rangle \sim (\hbar/g\mu_B T_2^*)^2 \exp(-|t-t'|/T_c)$, where $T_c \gg T_2^*$ is the correlation time of the nuclear spins.

Within this model, the random phase accumulated during an echo sequence ($\delta\phi = (g\mu_B/\hbar) \int_0^{\tau/2} \tilde{B}(t) dt - \int_{\tau/2}^{\tau} \tilde{B}(t) dt$) is characterized by its variance, $\langle \delta\phi^2 \rangle \approx \tau^3/[6T_c(T_2^*)^2]$ for $T_c \gg T_2^*, \tau$. Applying this model to an n_c -cycle CPMG sequence gives $\langle \delta\phi^2 \rangle \sim (n_c\tau)^3/[24n_c^2 T_c(T_2^*)^2]$. Thus, the multiple-pulse sequence yields an improvement in the lifetime by $(2n_c)^{2/3}$ (ref. 32). The improvement is conditional on $\tau, T_2^* \ll T_c$ and on the total interrogation time $n_c\tau$ being less than the relaxation time of the electron spins. Recent experiments have shown that the relaxation time in ultrapure samples is $\gg 20$ ms (ref. 18), suggesting $n_c \gtrsim 40$ cycles can result in an $(2n_c)^{1/3} \gtrsim 4$ overall improvement in sensitivity. Note that in practice this improvement will be limited by imperfections in the control pulses. For example, π -pulse errors of order 1% will limit $n_c \approx 25$, resulting in the optimal sensitivity shown in Fig. 2.

MEASUREMENT EFFICIENCY

The state of the electronic spin is measured by spin-selective fluorescence. When illuminated by green light, nitrogen-vacancy centres in the $m_s = 0$ state undergo a cyclic transition⁴⁵, with a rate limited by radiative decay ($\gamma \sim 15$ MHz). At the same time, centres in the $m_s = \pm 1$ state are rapidly pumped into a dark singlet state, from which they decay to the $m_s = 0$ state after a time $t_p \approx 0.5 \mu\text{s}$. To enable good discrimination of the $m_s = 0, \pm 1$ states, the measurement time t_m should be smaller than the optical pumping time t_p .

For a given photon collection efficiency η_m , an average of $\alpha_0 \approx (t_m\gamma)\eta_m$ photons are detected from each spin in the $m_s = 0$ state and $\alpha_1 (< \alpha_0)$ photons are detected from each spin in the $m_s = \pm 1$ manifold. We can estimate the combined effects of spin projection noise and photon shot noise for N measurements as $N^{-1/2}/C$, recovering the formulae for sensitivity used in the main text, with $1/C = \sqrt{1 + 2(\alpha_0 + \alpha_1)/(\alpha_0 - \alpha_1)^2}$. This includes the effects of photon shot noise and reduced contrast. For current experiments, a contrast $(\alpha_0 - \alpha_1)/(\alpha_0 + \alpha_1) \sim 0.3$ is observed. Efficiencies of $\eta_m \sim 0.001$ are achieved in current experiments^{15,18} and give $C \sim 0.05$. Assuming high collection efficiency ($\eta_m \gtrsim 0.05$) gives $C \sim 0.3$.

EFFECTS OF DIFFERENT NITROGEN-VACANCY-CENTRE ORIENTATIONS

To use an ensemble of nitrogen-vacancy centres as a vector magnetometer, the signal should originate from only one of the four different crystallographic axes. Under application of a d.c. transverse magnetic field $B_\perp \hat{x}$, the other (spectator) centres (with crystalline axis \hat{n}) have their $|\pm 1\rangle$ levels split by $g\mu_B B_\perp \hat{x} \cdot \hat{n}$. This detunes the spectator centres from the microwave field used for preparing and manipulating the $m_s = \pm 1$ subspace. For example, to use nitrogen-vacancy centres along the $(1, 1, 1)$ crystallographic axis, the ideal choice of \hat{x} is to align it with the $(1, 1, \bar{2})$ axis. We require the microwave Rabi frequency $\Omega \geq 3\pi/T_2^*$ for pulse errors to be smaller than our assumed measurement errors for the desired (111) axis. This translates to a requirement that $g\mu_B B_\perp > 3\hbar\Omega\sqrt{3}/2$ for the other three axes. For $T_2^* = 1 \mu\text{s}$, we require $B_\perp \geq 0.3$ mT. One intriguing development of nitrogen-vacancy-centre-based magnetometry would be to exploit the four crystallographic classes of nitrogen-vacancy centre to provide a full (three-dimensional) vector magnetometer, by changing the direction of the biasing transverse field B_\perp in between measurements.

Errors due to inhomogeneities in the nitrogen-vacancy-centre properties (for example, variations of the g -factor due to crystal strains) or to spatial inhomogeneities of the magnetic field can typically be neglected. Even for an average microtesla signal field and a distribution of g -factors or field inhomogeneity of order 4%, the induced dephasing leads to a broadening of the signal that is smaller than the effects of T_2 .

COUPLING TO PARAMAGNETIC IMPURITIES

The coupling of a nitrogen-vacancy electronic spin to other nitrogen-vacancy centres (S_k) and paramagnetic impurities such as nitrogen ($I_k, g_1 \approx g$) is given by the magnetic dipolar interaction. To first order in $1/\Delta$, the secular dipolar Hamiltonian is given by: $\mathcal{H}_{zz} + \mathcal{H}_{\text{cpr}}$, with $\mathcal{H}_{zz} = \sum_{jk} S_{z,j} \mathbf{D}_{jk} \cdot \hat{z}_k S_{z,k}$ and $\mathcal{H}_{\text{cpr}} = \sum_{jk} S_{z,j} \mathbf{D}_{jk} \cdot \mathbf{I}_k$. The dipole interaction vector is $\mathbf{D}_{jk} = (\mu_0 g^2 \mu_B^2 / 4\pi\hbar) ([3(\hat{r}_{jk} \cdot \hat{z})(\hat{r}_{jk} \cdot \hat{z})/\hat{r}_{jk}^3])$, with the \hat{z} axis set by the nitrogen-vacancy crystal axis of the sensing spin centres.

We model the secular component of the dipole coupling between paramagnetic impurities and nitrogen-vacancy centres as $\omega_{jk} = \mathbf{D}_{jk} \cdot \hat{x} I_x^k$ to the j th nitrogen-vacancy centre, and with a characteristic correlation time $t_c \approx \hbar/\sqrt{\langle D^2 \rangle}$: $\langle \hat{\omega}_{jk}(t) \hat{\omega}_{jk}(t') \rangle \approx \langle D^2 \rangle \exp(-|t-t'|/T_c)$. We can now calculate the expected spin-echo signal as a function of $\langle D^2 \rangle$, which scales as the square of the density of paramagnetic impurities. In this limit, when the correlation time and the interaction energy are at comparable scales, spin echoes decay exponentially as $\exp(-t/T_c)$. We find $T_c \approx 4/\sqrt{\alpha n^2}$; hence, for paramagnetic impurity densities of 10^{19} cm^{-3} , $T_c \approx 1 \mu\text{s}$.

At high densities, paramagnetic impurities and spectator nitrogen-vacancy centres may have sufficiently strong interactions to reduce the correlation time of the field-aligned component, I_x . Spectator nitrogen-vacancy centres may be optically pumped to their $m_s = 0$ state, reducing dynamical noise, reducing the effective temperature of the spectator system. However, spin echoes will not remove the effects of the paramagnetic impurities with short correlation times, and they may in fact limit the T_2 time and the corresponding bandwidth of the system. Experiments in systems with high nitrogen concentrations indicate exponential decay of echoes on a 5–20 μs timescale^{28,46} due to this coupling; more generally, the decay scales with the density of impurities. Although approaches such as CPMG and more complex decoupling may help, we anticipate that paramagnetic impurity concentrations below 10^{18} cm^{-3} will be necessary to achieve the best predicted sensitivities of this article.

NUMBER OF SPINS DETECTED BY A POINT-LIKE SENSOR

To estimate the number of spins that a localized sensor will detect, we determine the maximum and root-mean-square magnetic fields from a randomly distributed set of dipolar spins. We denote the dipolar field at a position \mathbf{r}_0 from a spin i as $\mathcal{G}\mathbf{b}(\mathbf{r}_i - \mathbf{r}_0, \mathbf{I}_i)$, with normalization of $\mathcal{G} = (g\mu_B \mu_0 / 4\pi) = B_H (10 \text{ nm})^3$ for protons and $\mathbf{b}(\mathbf{r}, \mathbf{I}) = (1/r^3)(\mathbf{I} - 3\mathbf{r}(\mathbf{r} \cdot \mathbf{I})/r^2)$ being the position dependence of the dipolar field (B_H is the magnitude of magnetic field created by a proton at a distance of 10 nm). The maximum detectable field occurs for polarized spins pointing perpendicular (z axis) to the surface (Fig. 4a). By symmetry, this field is parallel to the polarization, and we find

$$B_{\text{max}} = \mathcal{G} \left\langle \sum_i b_z(\mathbf{r}_i, \mathbf{I}_i) \right\rangle_{\text{pos}} = -2\pi\mathcal{G}I n_s,$$

where we choose coordinates such that the half-plane begins at $z = -r_0$, $\langle \rangle_{\text{pos}}$ averages over a homogeneous distribution of spin positions, and we assume a density n_s of dipolar spins, enabling us to replace the sum \sum_i with an integral $n_s \int_{z < -r_0} d^3r$. At high temperatures, the fluctuations of the potential values of the dipolar field reflect the \sqrt{N} noise statistics from a set of N spins. The mean-square of the z -component of the magnetic field is then:

$$\begin{aligned} B_{\text{r.m.s.}}^2 &= \mathcal{G}^2 \left\langle \sum_{ij} \langle b_z(\mathbf{r}_i, \mathbf{I}_i) b_z(\mathbf{r}_j, \mathbf{I}_j) \rangle_{\text{cfg}} \right\rangle_{\text{pos}} \\ &= \mathcal{G}^2 \frac{I(I+1)}{3} \left\langle \sum_i \frac{1}{r_i^6} \left(1 + 3 \frac{z_i^2}{r_i^2} \right) \right\rangle_{\text{pos}} \\ &= \mathcal{G}^2 \frac{I(I+1)}{3} n_s \frac{\pi}{2r_0^3}, \end{aligned}$$

where the average over spin configurations at high temperature uses $\langle I_{i,\mu} I_{j,\nu} \rangle_{\text{cfg}} = \delta_{\mu\nu} \delta_{ij} (I(I+1)/3)$. We find in particular that the statistical fluctuations are consistent with $B_{\text{r.m.s.}} \sim B_H \sqrt{N}$, where $N \sim n_s r_0^3$. More specifically, the effective number of spins detected N can be estimated from the relation $B_{\text{r.m.s.}} = |B_{\text{max}}|/\sqrt{N}$. Thus, $N = (|B_{\text{max}}|/B_{\text{r.m.s.}})^2 = (I^2/I(I+1)/3)(8\pi n_s r_0^3)$. For $I = 1/2$, this reduces to $N = 8\pi n_s r_0^3$, equivalent in effective detection volume to a half-sphere of radius $2.29r_0$.

Received 12 December 2007; accepted 15 August 2008;
published 14 September 2008; corrected online 1 February 2011

References

- Bending, S. J. Local magnetic probes of superconductors. *Adv. Phys.* **48**, 449–535 (1999).
- Chang, A. M. et al. Scanning Hall probe microscopy. *Appl. Phys. Lett.* **61**, 1974–1976 (1992).
- Budker, D. et al. Resonant nonlinear magneto-optical effects in atoms. *Rev. Mod. Phys.* **74**, 1153–1201 (2002).
- Auzinsh, M. et al. Can a quantum nondemolition measurement improve the sensitivity of an atomic magnetometer? *Phys. Rev. Lett.* **93**, 173002 (2004).
- Savukov, I. M., Seltzer, S. J., Romalis, M. V. & Sauer, K. L. Tunable atomic magnetometer for detection of radio-frequency magnetic fields. *Phys. Rev. Lett.* **95**, 063004 (2005).
- Kominis, K., Kornack, T. W., Allred, J. C. & Romalis, M. V. A subfemtotesla multichannel atomic magnetometer. *Nature* **422**, 596–599 (2003).
- Vengalattore, M. et al. High-resolution magnetometry with a spinor Bose–Einstein condensate. *Phys. Rev. Lett.* **98**, 200801 (2007).
- Zhao, K. F. & Wu, Z. Evanescent wave magnetometer. *Appl. Phys. Lett.* **89**, 261113 (2006).
- Mamin, H. J., Poggio, M., Degen, C. L. & Rugar, D. Nuclear magnetic resonance imaging with 90-nm resolution. *Nature Nanotech.* **2**, 301–306 (2007).
- Seton, H., Hutchison, J. & Bussell, D. A tuned SQUID amplifier for MRI based on a DOIT flux locked loop. *IEEE Trans. Appl. Supercond.* **7**, 3213–3216 (1997).
- Schlenga, K. et al. Low-field magnetic resonance imaging with a high- T_c DC superconducting quantum interference device. *Appl. Phys. Lett.* **75**, 3695–3697 (1999).
- Jezecko, F., Gaebel, T., Popa, I., Gruber, A. & Wrachtrup, J. Observation of coherent oscillations in a single electron spin. *Phys. Rev. Lett.* **92**, 076401 (2004).
- Jezecko, F. et al. Observation of coherent oscillation of a single nuclear spin and realization of a two-qubit conditional quantum gate. *Phys. Rev. Lett.* **93**, 130501 (2004).
- Hanson, R., Mendoza, F. M., Epstein, R. J. & Awschalom, D. D. Polarization and readout of coupled single spins in diamond. *Phys. Rev. Lett.* **97**, 087601 (2006).
- Childress, L. et al. Coherent dynamics of coupled electron and nuclear spin qubits in diamond. *Science* **314**, 281–285 (2006).
- Epstein, R. J., Mendoza, F. M., Kato, Y. K. & Awschalom, D. D. Anisotropic interactions of a single spin and dark-spin spectroscopy in diamond. *Nature Phys.* **1**, 94–98 (2005).
- Gaebel, T. et al. Room-temperature coherent coupling of single spins in diamond. *Nature Phys.* **2**, 408–413 (2006).
- Dutt, M. V. G. et al. Quantum register based on individual electronic and nuclear spin qubits in diamond. *Science* **316**, 1312–1316 (2007).
- Kühn, S., Hettich, C., Schmitt, C., Poizat, J.-Ph. & Sandoghdar, V. Diamond colour centres as a nanoscopic light source for scanning near-field optical microscopy. *J. Microsc.* **202**, 2–6 (2001).
- Chang, D. E., Sorensen, A. S., Hemmer, P. R. & Lukin, M. D. Quantum optics with surface plasmons. *Phys. Rev. Lett.* **97**, 053002 (2006).
- Meiboom, S. & Gill, D. Modified spin-echo method for measuring nuclear relaxation times. *Rev. Sci. Instrum.* **29**, 688–691 (1958).
- Salikhov, K. M. & Tsvetkov, Yu. D. in *Time Domain Electron Spin Resonance* (eds Kevan, L. & Schwartz, R. N.) (Wiley, New York, 1979).
- Maze, J. R., Taylor, J. M. & Lukin, M. D. Electron spin decoherence of single nitrogen-vacancy defects in diamond. Preprint at <<http://arxiv.org/abs/0805.0327>> (2008).
- Budker, D. & Romalis, M. Optical magnetometry. *Nature Phys.* **3**, 227–234 (2007).
- Khutsishvili, G. R. Spin diffusion. *Sov. Phys. Usp.* **8**, 743–769 (1966).
- Rabeau, J. R. et al. Implantation of labelled single nitrogen vacancy centers in diamond using ^{15}N . *Appl. Phys. Lett.* **88**, 023113 (2006).
- Meijer, J. et al. Generation of single color centers by focused nitrogen implantation. *Appl. Phys. Lett.* **87**, 261909 (2005).
- Charnock, F. T. & Kennedy, T. A. Combined optical and microwave approach for performing quantum spin operations on the nitrogen-vacancy center in diamond. *Phys. Rev. B* **64**, 041201R (2001).
- Hanson, R., Dobrovitski, V. V., Feiguin, A. E., Gywat, O. & Awschalom, D. D. Coherent dynamics of a single spin interacting with an adjustable spin bath. *Science* **320**, 352–355 (2008).
- Viola, L. & Lloyd, S. Dynamical suppression of decoherence in two-state quantum systems. *Phys. Rev. A* **58**, 2733–2744 (1998).
- Prins, J. F. Activation of boron-dopant atoms in ion-implanted diamonds. *Phys. Rev. B* **38**, 5576–5584 (1988).
- Slichter, C. P. *Principles of Magnetic Resonance* 3rd edn (Springer, Berlin, 1996).
- Mehring, M. *Principle of High Resolution NMR in Solids* (Springer, New York, 1983).
- Rey, A. M., Jiang, L., Fleischhauer, M., Demler, E. & Lukin, M. D. Many-body protected entanglement generation in interacting spin systems. *Phys. Rev. A* **77**, 052305 (2008).
- Khodjasteh, K. & Lidar, D. A. Performance of deterministic dynamical decoupling schemes: Concatenated and periodic pulse sequences. *Phys. Rev. A* **75**, 062310 (2007).
- Mansfield, P. Symmetrized pulse sequences in high resolution NMR in solids. *J. Phys. C* **4**, 1444–1452 (1971).
- Sekatskii, S. K. & Letokhov, V. S. Nanometer-resolution scanning optical microscope with resonance excitation of the fluorescence of the samples from a single-atom excited center. *JETP Lett.* **63**, 311–315 (1996).
- Chernobrod, B. M. & Berman, G. P. Spin microscope based on optically detected magnetic resonance. *J. Appl. Phys.* **97**, 014903 (2005).
- Degen, C. L. Scanning magnetic field microscope with a diamond single-spin sensor. *Appl. Phys. Lett.* **92**, 243111 (2008).
- Mamin, H. J., Budakian, R., Chui, B. W. & Rugar, D. Magnetic resonance force microscopy of nuclear spins: Detection and manipulation of statistical polarization. *Phys. Rev. B* **72**, 024413 (2005).
- Meriles, C. A. Optically detected nuclear magnetic resonance at the sub-micron scale. *J. Magn. Reson.* **176**, 207–214 (2005).
- Veauvy, C., Hasselbach, K. & Mailly, D. Scanning μ -superconduction quantum interference device force microscope. *Rev. Sci. Instrum.* **73**, 3825–3830 (2002).
- Maze, J. R. et al. Nanoscale magnetic sensing with an individual electronic spin in diamond. *Nature* doi:10.1038/nature07279 (2008).
- Balasubramanian, G. et al. Nanoscale imaging magnetometry with diamond spins under ambient conditions. *Nature* doi:10.1038/nature07278 (2008).
- Manson, N. B., Harrison, J. P. & Sellars, M. J. Nitrogen-vacancy center in diamond: Model of the electronic structure and associated dynamics. *Phys. Rev. B* **74**, 104303 (2006).
- van Oort, E., Manson, N. B. & Glasbeek, M. Optically detected spin coherence of the diamond N-V centre in its triplet ground state. *J. Phys. C: Solid State Phys.* **21**, 4385–4391 (1988).

Acknowledgements

We gratefully acknowledge conversations with D. Awschalom, A. Cohen, J. Doyle, G. Dutt, J. Maze, E. Togan, P. Stanwix, J. Hodges, S. Hong and M. P. Ledbetter. This work was supported by the NSF, ONR, MURI, DARPA and the David and Lucile Packard Foundation. J.M.T. is supported by the Pappalardo Fellowship; P.C. is supported by the ITAMP Fellowship.

Author information

Reprints and permission information is available online at <http://npg.nature.com/reprintsandpermissions>. Correspondence and requests for materials should be addressed to M.D.L.

High-sensitivity diamond magnetometer with nanoscale resolution

J. M. Taylor, P. Cappellaro, L. Childress, L. Jiang, D. Budker, P. R. Hemmer, A. Yacoby, R. Walsworth and M. D. Lukin

Nature Physics **4**, 810–816 (2008); published online 14 September 2008; corrected after print 1 February 2011.

In the version of this Article originally published, the x axis of Fig. 2b was labelled incorrectly, and should have appeared as shown below. This has now been corrected in the HTML and PDF versions.

